Ore Geology Reviews 138 (2021) 104344

Contents lists available at ScienceDirect

Ore Geology Reviews

journal homepage: www.elsevier.com/locate/oregeorev

Microscopic and NanoSIMS characterization of black shale-hosted pre-kinematic pyrites: Possible gold source of the orogenic gold deposits in the Truchas Syncline (Variscan Iberian Massif)

Fernando Gómez-Fernández [a,*], John K. Cunningham [b], Pablo Caldevilla [a], Antonio Herrero-Hernández [c], Andrew D. Beard [b]

[a] Área de Prospección e Investigación Minera, E.S.T.I. de Minas, Universidad de León, Avda. Campus de Vegazana s/n, 24007 León, Spain
[b] Department of Earth and Planetary Sciences, Birkbeck College, University of London, 9 Malet Street, London WC1E 7HX 10, United Kingdom
[c] Grupo de Investigación INGEOMAT, E.S.T.I. de Minas, Universidad de León, Avda. Campus de Vegazana s/n, 24007 León, Spain

ARTICLE INFO

Keywords:
Llamas de Cabrera gold district
Bacterial sulphate reduction
Framboidal pyrite
NanoSIMS maps
Sulphur isotopes
Variscan Orogen

ABSTRACT

The Truchas Syncline contains orogenic gold deposits (OGDs), hosted mainly by the Armorican Quartzite Fm. In order to look for the source of gold in these deposits, pre-kinematic sulphides from black shales from the overlying Luarca Fm. were studied using both optical and scanning electron (SEM) microscopy, as well as nanoscale secondary ion mass spectrometry (NanoSIMS). NanoSIMS images allowed the observation of relevant structures (pyrite with high As content nodules) hidden to SEM.

Microscopy and ^{36}S, $^{75}As^{32}S$, ^{75}As, $^{75}As^{34}S$, and ^{197}Au mappings, as well as $\delta^{34}S$ analysis (‰ Vienna-Canyon Diablo Troilite) allowed 4 types of pyrite to be characterized. According to their sequence of deposition, the pyrite types identified are the following: (1) framboid nuclei (FmPy), with $\delta^{34}S$ between +4.1‰ and +57.5‰; (2) overgrowths (OgPy), with presence of Au, As and $\delta^{34}S$ of approximately +20.5‰; (3) pyrite with high As content (AsPy), replacing previous pyrites, with $\delta^{34}S$ of approximately +23‰, nodular shapes and non-detected Au; (4) subhedral pyrite (ShPy), with $\delta^{34}S$ of approximately +19.7‰ and Au and As distribution showing (a) nuclei, (b) rims with Au and As and (c) structures interpreted as replacements of previous pyrite. Luarca Fm. pyrite framboids reach 75 μm in size, larger than framboids described in most previous NanoSIMS work, with microcrystals sufficiently large to be analyzed without contamination from edge effects. The FmPy formed in early diagenetic conditions by dissimilatory reduction of marine sulphate plus Rayleigh distillation or anaerobic oxidation of methane processes. The first FmPy nuclei formed in the periphery of framboids, and then started to form in the central region until completion of the framboidal structure. Growth of OgPy, AsPy and ShPy corresponded to more advanced diagenetic conditions, although the last stage of ShPy growth followed an aggregation model, in which ShPy metamorphic pyrites grew over ShPy diagenetic pyrites.

The sulphur isotopic signature of the four types of pyrite is in good agreement with a source from Ordovician marine sulphate. A hypothesis stating that the source of Au in OGDs in the district could be in Luarca Fm. is supported by the results of the present research. Firstly, a source of Au in the district could have been the replacement of previous pyrites by AsPy and the release of Au to the system, instead of the framboidal to euhedral pyrite recrystallization process observed in other gold deposits. Secondly, by the correspondence between $\delta^{34}S$ isotopic signature of the pyrites from Luarca Fm. and those from sulphides in OGDs. However, these results do not rule out other possible sources.

1. Introduction

Black shales are fine-grained sedimentary rocks enriched in organic carbon, in which the inorganic fraction may be of almost any composition (e.g., Huyck, 1990; Wignall, 1994; Ketris and Yudovich, 2009). They contain high metal contents (e.g., Shpirt et al., 2007; Parviainen

* Corresponding author.
E-mail addresses: f.gomez@unileon.es (F. Gómez-Fernández), j.cunningham@bbk.ac.uk (J.K. Cunningham), pcald@unileon.es (P. Caldevilla), aherh@unileon.es (A. Herrero-Hernández), ubfb018@mail.bbk.ac.uk (A.D. Beard).

https://doi.org/10.1016/j.oregeorev.2021.104344
Received 20 November 2020; Received in revised form 13 June 2021; Accepted 30 June 2021
Available online 6 July 2021

and Loukola-Ruskeeniemi, 2019). Their genetic relationship with metal ore deposits has been subject to debate in numerous mining districts (e.g., Coveney and Chen, 1991; Sáez et al., 2011; Polgári et al., 2012; Loukola-Ruskeeniemi and Lahtinen, 2013), including orogenic gold deposits (OGDs) and Carlin-type deposits (e.g., Shepherd and Bottrell, 1993; Bierlein et al., 2001; Mason et al., 2002; Large et al., 2011; Wu et al., 2020; Cunningham et al., 2019). Many trace metals in black shales are hosted by sedimentary/diagenetic framboidal to euhedral pyrite (e.g., Large et al., 2011, 2012; Gregory et al., 2015; Zhao et al., 2018; Wu et al., 2020) deposited in oxygen deficient conditions in different environments, from marine water columns to diagenetic conditions (e.g., Lyons, 1997; Raiswell and Canfield, 1998; Lin et al., 2016b, 2017).

In sedimentary marine/diagenetic environments, the formation of framboidal pyrite is related mainly to the activity of sulphate-reducing bacteria and also with the activity of archaea (e.g., Brunner and Bernasconi, 2005; Lin et al., 2016b; Jørgensen et al., 2019) in the sulphate–methane transition zone. The size of framboids has been related to redox conditions in the sedimentary environment in which they grow (Wilkin et al., 1996; Wei et al., 2016). However, Lin et al. (2016b) and Rickard (2019) argued the size of framboids may be conditioned by many other factors.

Dissimilatory sulphate reduction, linked to the activity of bacteria in presence of electron-accepting organic substrata, releases H_2S, which is highly depleted isotopically compared to the precursor sulphate, to the extracellular medium (e.g., Donald and Southam, 1999; Rudnicki et al., 2001; Brunner and Bernasconi, 2005; Sim et al., 2011). Depletions ($\delta^{34}S_{sulphate\text{-}sulphide}$) are usually between 2‰ and 46‰, and can be as much as 75‰ (Wortmann et al., 2001; Canfield et al., 2010; Sim et al., 2017), and even 135‰ in high temperature conditions (Rudnicki et al., 2001). Large $\delta^{34}S_{sulphate\text{-}sulphide}$ values have been attributed to a combination of reduction, oxidation and microbial sulphur disproportionation cycles (Canfield and Thamdrup, 1994; Habicht et al., 1998; Böttcher and Thamdrup, 2001). Later formation of iron monosulphides from H_2S generates fractionations usually lower than 1.5‰; and the transformation of these monosulphides into pyrite also shows very low fractionations (Price and Shieh, 1979; Böttcher et al., 1998).

High $\delta^{34}S$ in framboidal pyrites has been traditionally interpreted as a result of Rayleigh distillation processes, produced in closed-system conditions, in which the remaining sulphate-sulphur in the fluid becomes heavier and heavier as the sulphides precipitate (Canfield and Teske, 1996; Rudnicki et al., 2001; Gregory et al., 2019; Jørgensen et al., 2019). Prevalence of these conditions through time will generate a wide range of isotopic values in the new sulphides (Ohmoto and Goldhaber, 1997), with $\delta^{34}S$ increases of up to 100‰ and variations of up to 60‰ over 50 μm in a single pyrite crystal (Drake et al., 2015).

Anaerobic oxidation of methane in ascending methane flows coupled to dissimilative sulphate-reducing bacteria processes have been described (hereafter S-AOM) involving strong sulphur isotope fractionation (Borowski et al., 2013; Deusner et al., 2014; Magnall et al., 2016; Lin et al., 2016b, 2017; Jørgensen et al., 2019). All these papers report the presence of pyrite very enriched in $\delta^{34}S$, related to S-AOM, with $\delta^{34}S$ range from −41.6 to +114.8‰ (Lin et al., 2016b). Presumably, S-AOM is catalyzed by associations of methanotrophic archaea and sulphate-reducing bacteria (Hinrichs et al., 1999; Pancost et al., 2000; Knittel and Boetius, 2009). In columns of recent marine sediments dissimilatory sulphate reduction dominates within the first meters, and S-AOM dominates with depth (Lin et al., 2016b). Most of the methane that is diffused upwards is consumed coupled with sulphate reduction in the sulphate–methane transition zone, where pore water sulphate and methane concentrations are reduced almost to zero (e.g., Yoshinaga et al., 2014; Lin et al., 2016b; Jørgensen et al., 2019) as the dissolved hydrogen sulphide reaches its highest concentration (Boetius et al., 2000; Reeburgh, 2007). Accordingly, deeper into the sediments from the seabed, sulphate $\delta^{34}S$ gets increasingly heavier (sulphate-reduction zone), until it reaches its maximum values when reaching the sulphate–methane transition zone, and then decreases below it (Lin et al., 2016b).

Regarding pyrite behaviour during diagenesis and metamorphism, the literature reports the evolution of pyrite from framboidal to euhedral shapes and, ultimately, to pyrrhotite (e.g., Pitcairn et al., 2006; Large et al., 2007, 2012; Tomkins, 2010; Zhao et al., 2018). According to Large et al. (2011), in each of these transformations, gold and other metals are released to pore waters, which forms the basis of the genesis of Carlin deposits and OGDs where sedimentary rocks host the mineralisation and particularly where carbonaceous mudstones form a significant component of basin sediments.

OGDs, extensively mined during the Roman Empire (Herail, 1984; Matías and Gómez-Fernández, 2003), are found in the Truchas Syncline (Fig. 1). According to Gómez-Fernández et al. (2012), gold and other metals in OGDs were deposited in extensional quartz veins with three hydrothermal stages: As–Fe (I), As–Fe (II), and Au–Zn–Cu–Pb, to which a later supergene alteration stage was superimposed.

$\delta^{34}S$ values of the two As-Fe stages are similar, +8.0‰ to +19.5‰, whereas sin-kinematic pyrites from siliciclastic Luarca Fm. show higher variability, from +7.4‰ to +26.3‰. Calculated $\delta^{18}O$ data for the fluids, as well as fluid inclusion data, suggest that mineralizing fluids were equilibrated with metamorphic lithologies at mezozonal temperatures (Groves et al., 1998). The source of gold, according to the metamorphic model for OGDs, is in chlorite devolatilization in the transition zone between greenschist/amphibolite facies (Goldfarb and Groves, 2015; Zhong et al., 2015). However, Gómez-Fernández et al. (2019) propose the pre-kinematic pyrite of the Luarca Fm. as a gold source. The metamorphic grade of this formation is greenschist, with chlorite present in the silicate assemblages, clearly a shallower source at a lower metamorphic grade than the metamorphic model (op.cit).

In black shales from Luarca Fm. in the Truchas Syncline (Fig. 1) graphite and several generations of pyrite are present, from framboidal to euhedral (Gómez-Fernández et al., 2009a; Cárdenes et al., 2016). According to Gómez-Fernández et al. (2019), the source of gold in the Truchas Syncline OGDs is, at least partly, from the pyrites of this formation. In that study, metal contents in both graphite and pyrite from Luarca Fm. have been determined by electron microprobe, with average Au and As levels of 217 and 1999 ppm respectively for framboids. Moreover, $\delta^{34}S$ was determined in pyrites with grain size large enough to enable the application of traditional methodologies (Robinson and Kusakabe, 1975). However, these techniques cannot be applied to the grain sizes of the microcrystals which make up the pre-kinematic framboidal pyrite (usually between 3 and 5 μm) and its subhedral derivatives.

The present work aims to broaden the research started by Gómez-Fernández et al. (2019) at a more detailed scale. For this purpose, nanoscale secondary ion mass spectrometry (NanoSIMS) was applied, which allowed: a) geochemical mapping on pre-kinematic pyrites from the Luarca Fm. and, b) determination of the isotopic signatures ($\delta^{34}S$) of framboidal to subhedral pyrites.

The present contribution provides information on: (1) the application of NanoSIMS to auriferous framboidal pyrite, (2) the genesis and evolution of the pyrites from the Luarca Fm. and (3) the origin of gold in the Truchas Syncline OGDs.

2. Geological setting

The sedimentary sequence in the study area starts, from the bottom to the top, with Capas de los Montes (schists, Lower Ordovician) and Armorican Quartzite (Lower to Middle Ordovician). On top of the latter, the Capas de Transición have been defined (not shown in the map of Fig. 1), formed by a sequence of quartzites and shales, over which the Luarca Fm. lies (black shales with intercalations of volcanic rocks; Middle Ordovician). The composition of these volcanic rocks is mainly basaltic, with minor acid intercalations, and occurs as volcanic-volcanoclastic layers (González-Menéndez et al., 2021). Upper Ordovician is composed of a mainly siliciclastic sequence (Barros Lorenzo,

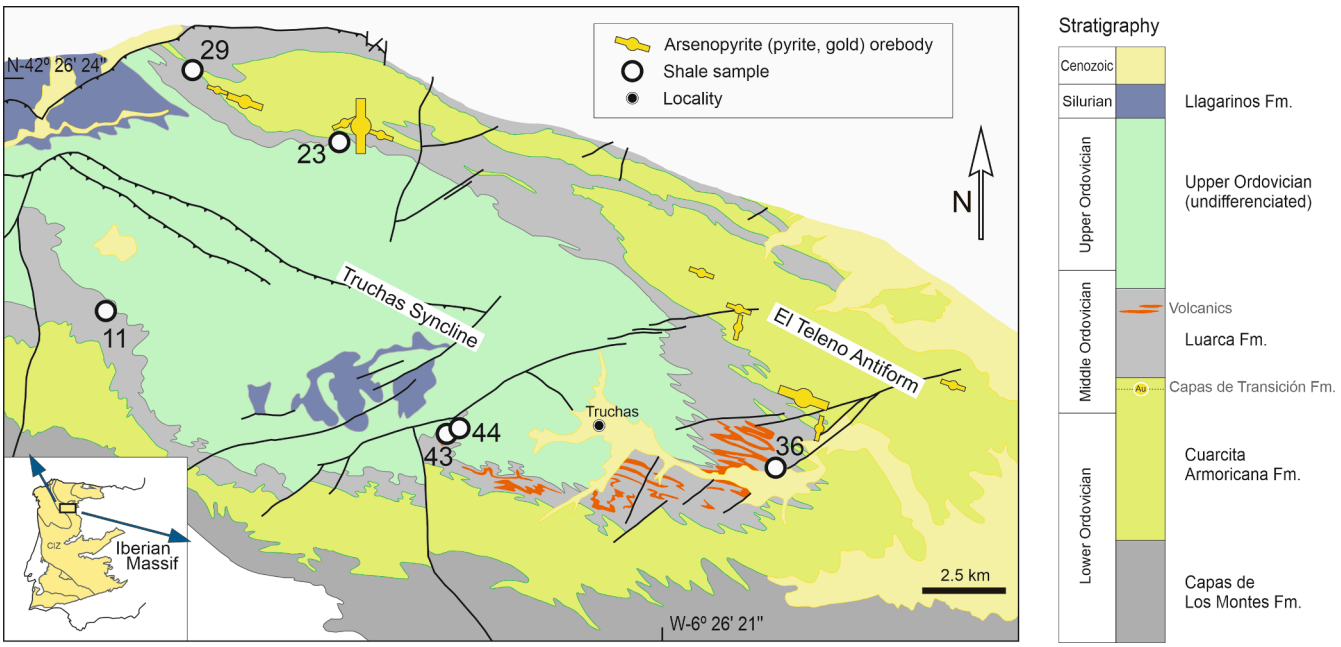

Fig. 1. Geological map of the Truchas Syncline (modified after Suárez et al., 1994; González-Menéndez et al., 2021), with location of samples and OGDs.

1989; Voldman and Toyos, 2019), with abundant black shales, whose mineralogy and petrology, along with those of Luarca Fm, have been widely studied (Ward and Gómez-Fernández, 2004; Gómez-Fernández et al., 2009a, 2009b, 2017; Cárdenes et al., 2014), as they form the most important roofing slate mining district in the world. The Palaeozoic sequence ends with shales rich in organic matter (Llagarinos Fm.; Silurian).

From a structural point of view, the study area is part of the Truchas Syncline, a geological structure that lies in the Central Iberian Zone, within the Iberian Variscan Massif (Fig. 1). It was formed as a result of the coaxial interference of Variscan phases 1 and 3, and was affected by south-north trending thrusts, developed during the second Variscan phase (Marcos, 1973; Pérez-Estaún, 1978). The first phase of deformation gave rise to a widespread penetrative tectonic foliation (S_1). In local areas, a crenulation schistosity is also present, associated with the third phase of deformation. Variscan regional metamorphism reached greenschist facies.

Primary OGDs are found in the northern limb of the Truchas Syncline and in the Teleno Anticline (Fig. 1), hosted in the upper part of the Armorican Quartzite and occasionally in the overlying shales from Luarca Fm. (Tornos et al., 1997; Gómez-Fernández et al., 2012; Cunningham et al., 2019).

3. Sampling and analytical procedures

Thin sections of Luarca Fm. shale samples, collected in quarries and in outcrops (Ward and Gómez-Fernández, 2004; Gómez-Fernández et al., 2019) were made for study using optical microscopy and scanning electron microscopy (SEM). A JEOL JSM-6480 scanning electron microscope (JEOL, Akishima, Tokyo), equipped with an Oxford D6679 Energy-dispersive X-ray spectroscopy (EDS) detector, and an Olympus BX51 petrographic microscope (Olympus, Shinjuku-ku, Tokyo), equipped with an Olympus Camedia C-5050 Zoom lens double bed, were used for this purpose. Sample 29 (Fig. 1) containing both framboidal and subhedral pyrite, was selected for study using NanoSIMS. Portions of this sample were embedded in an epoxy resin and eight cylindrical polished mounts were made, with dimensions of 1 in. in diameter and 5 to 7 mm in height.

Selected framboidal pyrites were analysed using the CAMECA NanoSIMS 50L at the Open University (Planetary and Space Sciences, Milton Keynes, UK) for high-resolution trace element imaging and in situ sulphur isotopic spot analyses. Two mounts containing framboidal to subhedral pyrites were polished using 1/4 μm as the end diamond size and then coated with carbon for conductivity. Sample areas of 30*30 μm^2 were pre-sputtered using a 100pA primary beam for 5 min to remove the carbon layer and possible surface contamination. A 10pA focused Cs^+ primary beam with a diameter of 300 nm and accelerating voltage of 16 kV was used to scan over 20*20 μm^2 sample regions within the pre-sputtered area to carry out the trace element images. Negative secondary ions of ^{36}S, ^{75}As, $^{75}As^{32}S$, $^{75}As^{34}S$ and ^{197}Au were collected simultaneously using electron multipliers. Each imaging analysis contained 30–60 frames, and a frame size of 256*256 pixels was used for all images with an integration time of 1000 ms per pixel, leading to a measurement time of 20–40 min for each image. All image data were corrected for detector dead time and aligned for possible stage shift. The literature reports a lack of appropriate standard materials for the elements of interest (Au and As) with secondary ion mass spectrometry (SIMS)-based methods (Wiedenbeck, 2012; Zhang et al., 2017; Gregory et al., 2019) and therefore the data is given in counts per pixel of the NanoSIMS map. The colour scale for each image was adjusted to show the range between maximum and minimum value in the image. Therefore, direct comparisons of colours between equivalent images from different regions are possible given that their orders of magnitude are similar and that the mineral mapped was always pyrite. Count rates for As were all high compared to any background or dark noise contribution. Au count rates were sometimes below detection limits, with the lowest measured $Au/^{36}S$ ratio reported of $1.5E^{-5}$ approaching detection limit.

Subsequent to the trace element imaging analyses, selected single pyrite grains from three imaging regions were measured using a 5pA focused Cs^+ primary beam for in situ sulphur isotopic spot analyses using a modified protocol based on Zhang et al. (2014). Negative secondary ions were collected simultaneously using electron multipliers (^{33}S, ^{34}S, ^{36}S and ^{75}As) and Faraday cup (^{32}S) from 2*2 μm^2 areas. Each spot analysis contained 200 measurements, with a total analysis time of 2 min. A mass resolution power of 8000 (CAMECA definition) was used for both trace element imaging and sulphur isotope spot analyses, which was enough to resolve possible mass interferences such as $^{32}SH_2$ and $^{33}SH^-$ on $^{34}S^-$. Two pyrite standards at the Open University (OU-Pyrite-D and OU-Pyrite-E) were used as working references to correct for matrix

effects and instrumental mass fractionation. The $\delta^{34}S$ of the standards were measured using the method of Robinson and Kusakabe (1975) at the Stable Isotope Laboratory of the University of Salamanca and relative to the Vienna-Canyon Diablo Troilite (V-CDT).

In one of the 20*20 μm^2 mapped regions, 10 of the 2*2 μm^2 square areas and in the irregular shaped Au rich areas, $^{75}As/^{36}S$ and $^{197}Au/^{36}S$ ratios were quantified. As no suitable standard with known Au or As concentrations was available, the As/S and Au/S ratios are the uncorrected measured values and only provide relative concentrations to each other. As the mineral analysed was always pyrite, there should be little or no matrix effect and therefore the results from different samples are directly comparable.

4. Results

4.1. Optical and scanning electron microscopy

The main minerals in black shales from the Luarca formation are muscovite, quartz, chlorite and albite (details can be seen in Gómez-Fernández et al., 2009a, 2009b). Accessory minerals include pyrite, chalcopyrite, galena, sphalerite, graphite, ankerite, rutile, zircon, monazite, xenotime and apatite.

Regarding the Variscan deformation that affected the region, two groups of sulphides have been identified:

- Group I) Pre-kinematic sulphides, appearing as framboids or as part of porphyroidal aggregates (Pk, in Fig. 2A-B) together with quartz and phyllosilicates. Pyrite is the most common sulphide, and appears with minor galena and chalcopyrite. Research presented in this paper focused on pyrites of this first group of sulphides.

The sulphides show polyphasic pyrite growth, from framboidal to subhedral habits (Fig. 3A). The following types of pyrite were identified: a) framboidal microcrystals of pyrite (FmPy), which constitute the nuclei of the framboids, with oval to polyhedral sections (Fig. 3B), mainly equidimensional, equimorphic and following regular spatial ordering patterns (Ohfuji et al., 2005), b) pyrite overgrowths (OgPy) surrounding FmPy (Fig. 3C) and, c) subhedral to euhedral pyrite (ShPy) (Fig. 3D). Galena and chalcopyrite are found as well, in very scarce small crystals (Fig. 2C-F, 3D-F), more frequently in association with ShPy. In framboids, galena may appear associated with FmPy (Fig. 2C-D), with OgPy (Fig. 3E) or crosscutting framboid inner structure (Fig. 3F). None of the shales studied, frequently used as commercial roofing slate, shows signs of hydrothermal activity.

The framboids size usually ranges from 35 and 50 μm (Fig. 2C-F, 3A and F) and can reach up to 75 μm (framboid from the S4_1 and 2 regions, Fig. 5). They appear to be surrounded by S_1 tectonic foliation (Fig. 2C-D), marked by chlorite and muscovite orientation. Associated with these framboids, pressure shadows (Ps) are observed, elongated parallel to foliation, in which quartz dominates over chlorite and muscovite. As a general rule, ShPy appears within the porphyroidal aggregates around which S_1 flows. Nevertheless, occasionally (Fig. 2E-F) foliation is cut by outer parts of ShPy crystals (yellow arrows in Fig. 2F).

All of the above reveals the pre-kinematic character of polyphasic pyrite overgrowths, although the last phase of ShPy growth is very likely to be sin-kinematic.

- Group II) Sin-kinematic sulphides (Sk, in Fig. 2G-H) are the dominant pyrite type. They usually crosscut the S_1 foliation and have associated pressure shadows, which indicates that they formed prior to the final stages of the Variscan deformation. They are almost entirely pyrite, with some minor and very scarce galena and chalcopyrite. Pyrite forms euhedral to subhedral individual crystals, very often in cubic shapes, and may reach sizes of up to several centimetres long on each side.

4.2. NanoSIMS studies

NanoSIMS studies were undertaken on pre-kinematic pyrites in sample 29, from framboidal to subhedral. ^{36}S, $^{75}As^{32}S$, ^{75}As, $^{75}As^{34}S$, and ^{197}Au mappings were performed on 7 different 20*20 μm^2 regions (e.g., Fig. 4).

Furthermore, 27 $\delta^{34}S_{(V\text{-}CDT)}$ isotopic determinations in three of the seven analysed regions were conducted, which generated square depressions of 2*2 μm^2 (regions S4_1, S4_2 and S8_9_1; Fig. 5). In 10 of these square areas (region S4_2; Fig. 6), $^{75}As/^{36}S$ and $^{197}Au/^{36}S$ ratios were quantified. These same ratios were also determined as bulk composition of most of the Au rich areas with irregular shapes (Analysis 11 in Fig. 6; Table 1).

NanoSIMS maps show structures that were unable to be seen on the backscattered electron (BSE) images previously acquired with SEM (Figs. 4 and 5). ^{36}S distribution NanoSIMS maps appear very saturated in all the regions analysed (Fig. 4B), showing diffuse structures that are maximized in the Au and As distribution maps.

In addition, in each of the analysed regions, the three different maps involving As distribution ($^{75}As^{32}S$, ^{75}As, $^{75}As^{34}S$) are very much alike (Fig. 4), thus permitting a joint interpretation. Therefore, in Fig. 5 only the $^{75}As^{32}S$ mappings are presented.

The Au and As contents which we refer to in the following paragraphs are relative contents of ^{36}S, $^{75}As^{32}S$, ^{75}As, $^{75}As^{34}S$ and ^{197}Au, graphically expressed on the images or numerically through the $^{75}As/^{36}S$ and $^{197}Au/^{36}S$ ratios (Table 1). In the $^{75}As^{32}S$ mappings a range of 4 colours with metallogenetic significance were distinguished. From lower to higher As content they are: a) dark blue, b) light blue, c) green-yellow and d) orange. This observation, along with the crystal shape, the Au contents (^{197}Au mapping) and the isotopic ratios of sulphur (Table 1 and Fig. 5A–C), allowed us to differentiate, in addition to the three types of pyrite previously identified through SEM, a fourth type, characterized by its high As content. These four types are the following:

a) FmPy. It forms the nuclei of the framboids (Fig. 5D-F). It is characterized by low As content (dark blue), by the absence of observable Au (Fig. 5G-I) and, especially, by a strong diversity in the sulphur isotopic distribution, with $\delta^{34}S$ from +4.1‰ to +57.5‰ (Table 2).
b) OgPy. It covers the FmPy and it is characterized by slightly higher As contents (green-yellow colours; Fig. 5D-F) and presence of Au (Figs. 4, 5G-I and 6). The sulphur isotopic signature is quite constant, with $\delta^{34}S$ values of approximately +20.5‰ (Table 2).
c) Pyrite with high As content (AsPy), forms nodules, apparently more varied in size and with a more heterogeneous distribution than FmPy nuclei (Fig. 4C-E, 5D-F). It often cuts the contacts between FmPy and OgPy pyrites which can be interpreted as evidence of replacement (see section 5.1). It is characterized by the highest As content among all those analysed, reflected by the orange colours in the figures. The images did not register significant counts of Au in the AsPy (Fig. 5G-I and 6). The sulphur isotopic signature in AsPy is quite constant with $\delta^{34}S$ values around +23.0‰ (Table 2).
d) ShPy. The sulphur isotopic signature for ShPy is quite constant, with $\delta^{34}S$ values around +19.7% (Table 2). The mapping and distribution of the As contents reveals 3 different structures (Fig. 5): (1) nuclei (n), less rich in As (light blue colours) and Au, (2) rims (rm), slightly higher in As (green-yellow and occasionally orange colours) and Au, equivalent to those in OgPy (Fig. 5G-I) and, (3) closed structures (rp), with low As content nuclei (light blue colours) and rims with slightly higher As contents (yellow colours; Fig. 5D-E) which are interpreted as a result of the replacement of previous pyrites (see Discussion in section 5.1). On the other hand, in some localized areas (white arrow in Fig. 5D), of irregular limits, As contents are equivalent to those in FmPy.

There is a noticeable difference between $\delta^{34}S$ in the FmPy and the other types of pyrite (Figs. 5 and 7C, Tables 1 and 2). In FmPy, $\delta^{34}S$ data are very heterogeneous, and in some cases very heavy. Nevertheless, in each of the other three types of pyrite the values are very homogeneous and, in the three as a whole, rather similar. Highest, lowest and mean values, as well as the standard deviation for every type are shown on

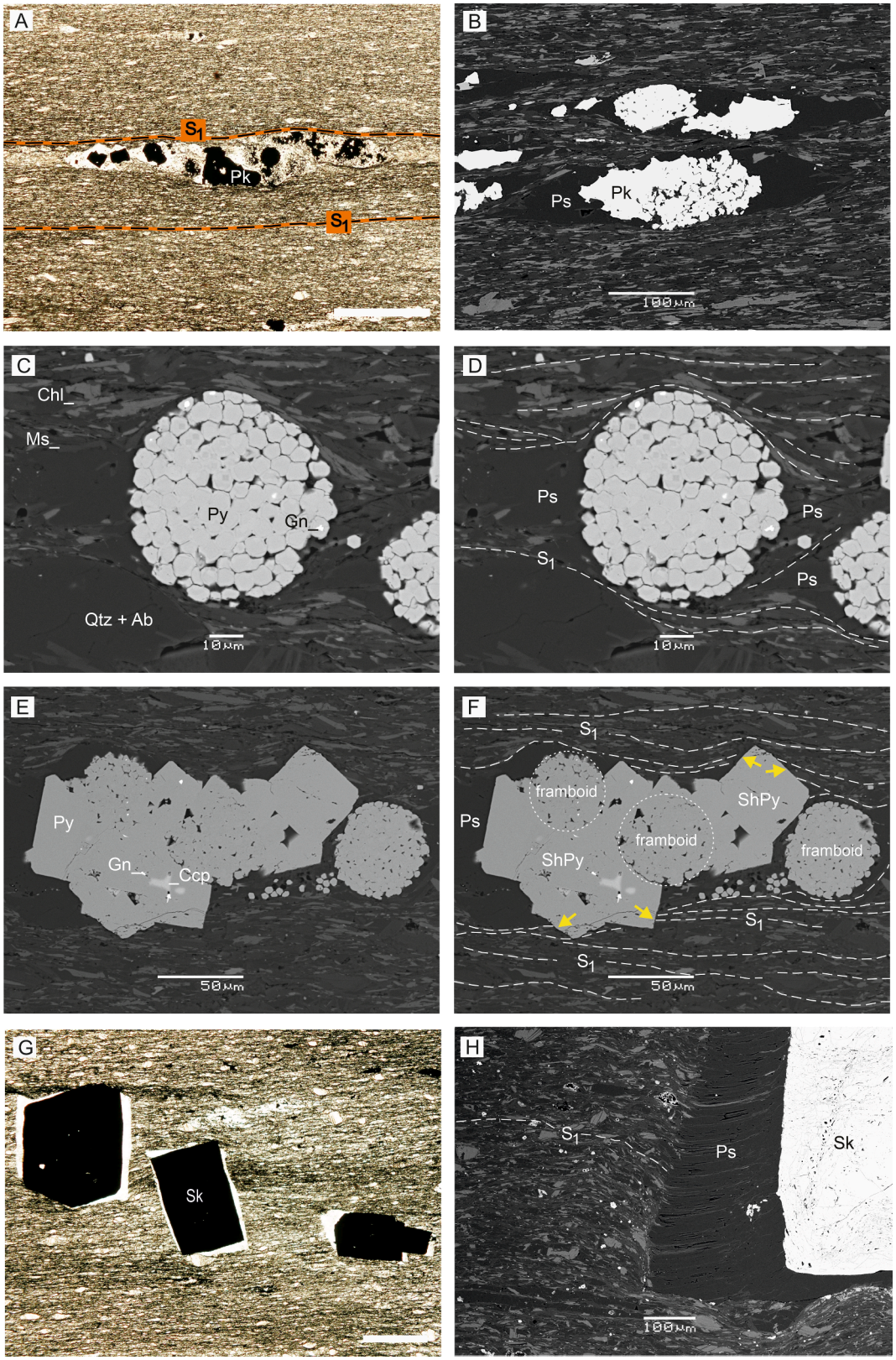

Fig. 2. Microphotographs and backscattered electron (BSE) images showing different types of pyrites and their relationship with the tectonic foliation (S_1). A and B) Pre-kinematic porphyroidal aggregates formed by sulphides (Pk) and quartz, outlined by S_1. C and D) Framboidal pyrite outlined by S_1. E and F) Porphyroidal aggregate with FmPy to ShPy, in which S_1 is locally cut through by ShPy (areas with yellow arrows). G and H) Euhedral to subhedral sin-kinematic pyrites (Sk), crosscutting S_1 and showing pressure shadows. A and G) microphotographs: plane polarized light; scale bar = 0.5 mm. B to F, and H) BSE images. Chl = chlorite; Ms = muscovite; Qtz = quartz; Ab = albite; Py = pyrite; Ccp = chalcopyrite; Gn = galena; Ps = pressure shadows. Samples: 29 (A, and C to F), 11 (B), 44 (G and H).

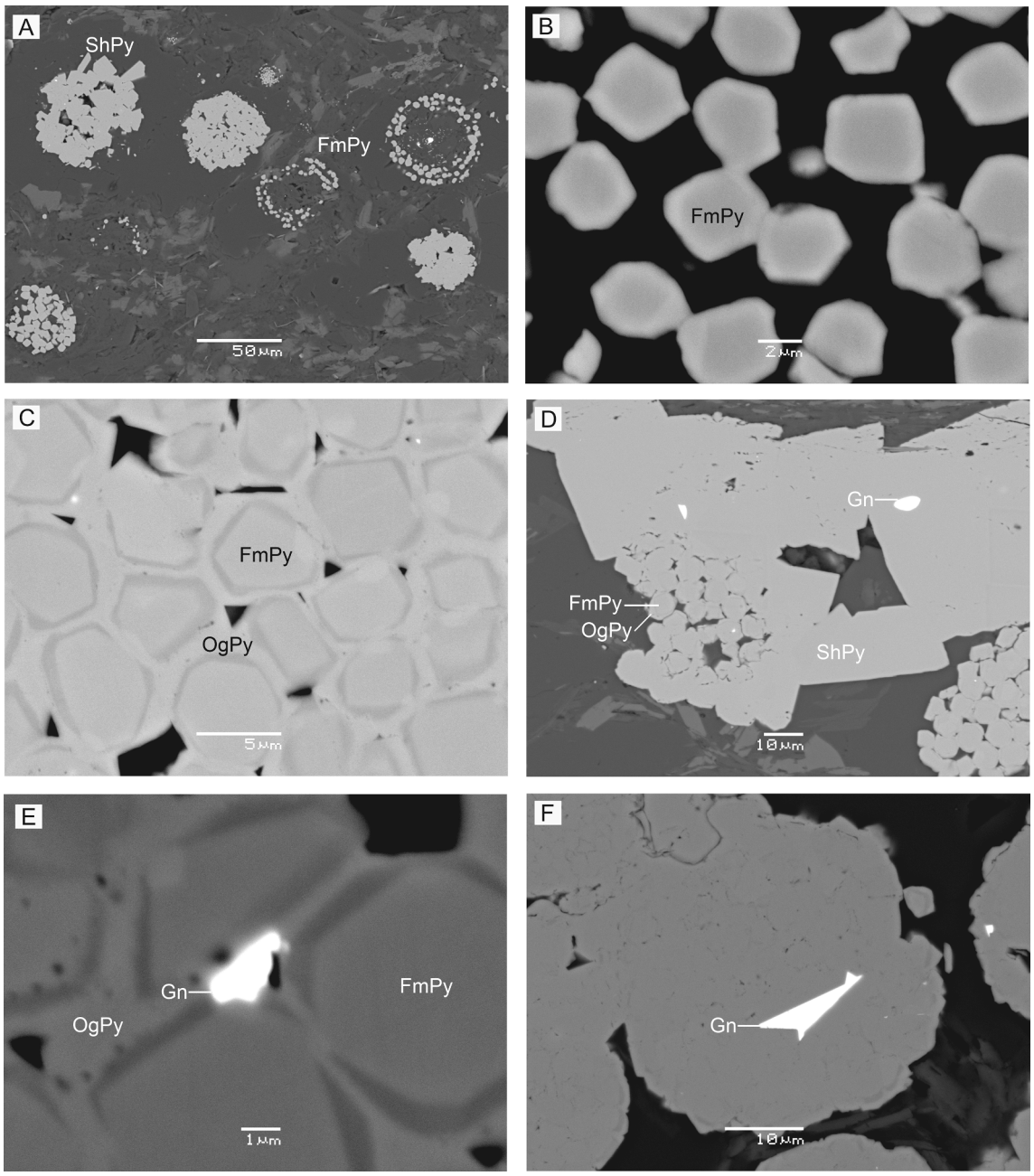

Fig. 3. BSE microphotographs showing pre-kinematic pyrites, in different stages of growth, evolving from framboidal pyrite (FmPy), overgrowths (OgPy) into subhedral shapes (ShPy), and relation between Galena (Gn) and these types of pyrite.

Table 2.

5. Discussion

5.1. Paragenetic sequence

The first type of pyrite to form was FmPy (Fig. 3B), over which OgPy overgrowths developed (Fig. 3C). An alternative interpretation, considering AsPy as the first type of pyrite to form, fails to explain the following facts: (1) AsPy often cuts the contacts between FmPy and OgPy (Fig. 5D to F), therefore it must be after these two and (2) the first crystals to form in framboids (Fig. 3B) are basically equidimensional, equimorphic and following regular spatial ordering patterns (Ohfuji and Rickard, 2005), properties more commonly found in FmPy than in AsPy (Fig. 3B-C and 5F).

Regarding ShPy, As contents allowed differentiation of nuclei (n) and rims (rm) (section 4.2) and interpretation that closed structures, nearly circular (rp), occasionally appearing in the outer part of the framboids (rp in Fig. 5D and E) correspond to replacements of FmPy and OgPy by ShPy. As a consequence of this replacement, the contacts between what was FmPy and OgPy were blurred (e.g., Fig. 5B).

AsPy replaces FmPy and OgPy, implying it formed later. However, AsPy has not been observed superimposed on ShPy, thus it is very likely to have formed earlier than ShPy. For AsPy to be younger than ShPy requires AsPy to have selectively replaced FmPy and OgPy, and not ShPy. The images did not register significant counts of Au in the AsPy (Fig. 5G-I), not even in those areas where replaced pyrite presumably contained Au (e.g., AsPy nodules subjected to analysis: number 1 in Fig. 5H and numbers 7 and 8 in Fig. 5I). Therefore, we interpret that replacement of previous pyrites by AsPy could have released Au to the

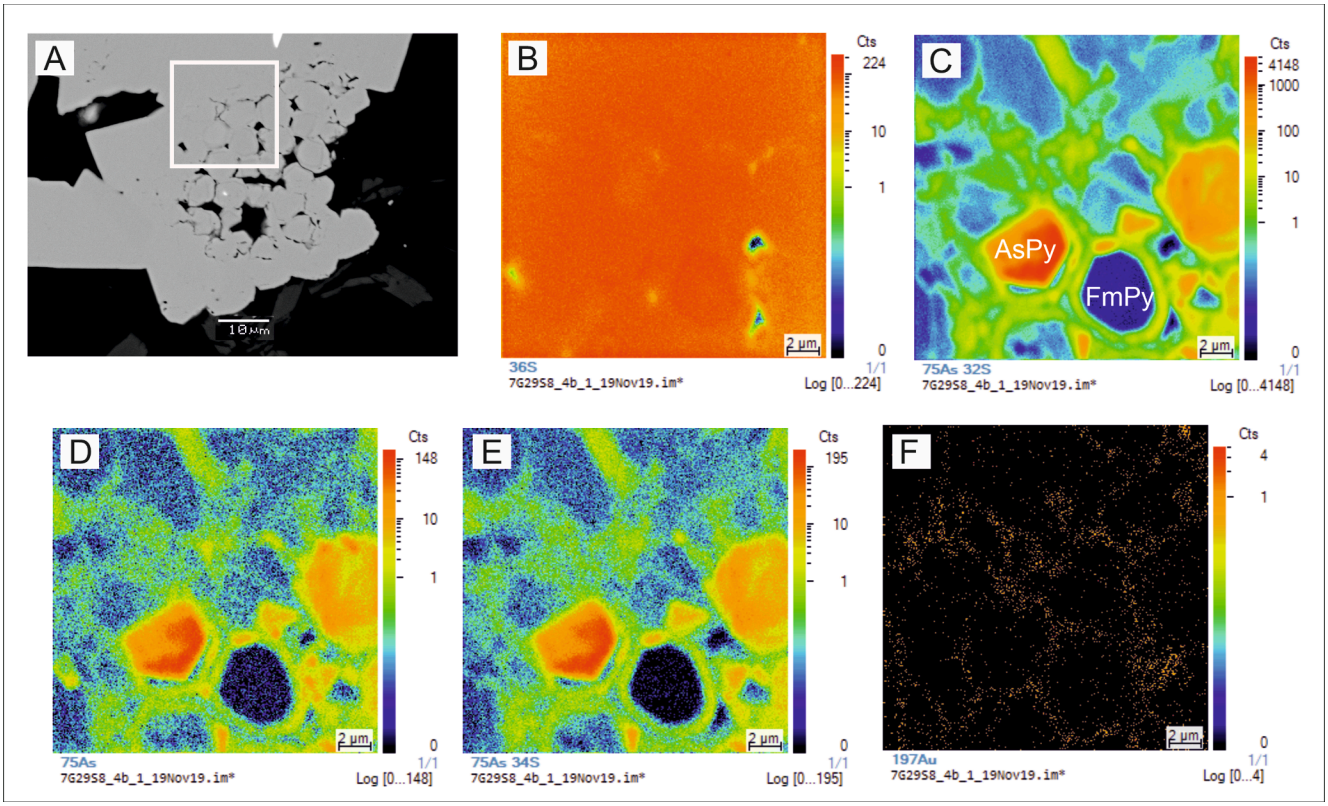

Fig. 4. BSE image (A) and NanoSIMS maps of distribution of ^{36}S (B), $^{75}As^{32}S$ (C), ^{75}As (D), $^{75}As^{34}S$ (E) and ^{197}Au (F) in the region S8_4b_1. A) BSE image indicates the area mapped in the rest of the images.

mineralising processes.

Fig. 7 outlines the growth phases for each type of pyrite, and also the paragenetic sequence and the $\delta^{34}S$ isotopic signature.

5.2. *Pyrite precipitation: geological environments*

Geometric relationships between the tectonic foliation and the pressure shadows with the pyrite framboids (Fig. 2D) indicates the pre-kinematic character of the latter. Therefore framboids must have formed prior to the first phase of Variscan deformation, which places their formation in a diagenetic/sedimentary environment. Sequences of framboidal to overgrowths and subhedral pyrites, as described in this work, have been reported in sedimentary/diagenetic conditions on multiple occasions (e.g. Sawlowicz, 1993; Wei et al., 2012; Ding et al., 2014; Lin et al., 2016b).

In FmPy, $\delta^{34}S$ values range between +4.1‰ and +32.4‰ in the outer nuclei of one of the analysed framboids (S4_1 and S4_2 regions, Fig. 5). In the second framboid (S8_9_1 region), in which several nuclei from the edge to the centre of the framboid were analysed, $\delta^{34}S$ values offer the following succession: +35.8‰, +44.1‰, +42.4‰, +57.5‰ and +46.3‰ (Fig. 5, Table 1). We do not know the potential influence of the taxonomy of the bacterial strains or archaea involved in the genesis of framboids (Brüchert et al., 2001; Knittel and Boetius, 2009). Nevertheless, images in which framboids in different growth stages can be seen (Fig. 3A and 7A) show a tendency for the first nuclei to form groupings on the periphery of the framboid and then start to form in the central region until completion of the framboidal structure. Similar growth schemes were already identified by Sawlowicz (1993) and Lin et al (2016b), among others.

Mean $\delta^{34}S$ values in the analysed FmPy nuclei ($\delta^{34}S_{mean}$ = +28.4‰; Table 2), are similar to the isotopic signature of the Ordovician marine sulphate $\delta^{34}S$ ~ +28 to +30‰; (Claypool et al., 1980). Data from some nuclei, with $\delta^{34}S$ as light as +4.1‰ and therefore with depletions $\delta^{34}S_{sulphate\text{-}sulphide}$ = 16.9‰, can be explained by the marine sulphate reduction in the dissimilatory sulphate reduction zone (e.g., Brunner and Bernasconi, 2005; Canfield et al., 2010; Sim et al., 2017). Heavier values ($\delta^{34}S$ up to +57.5‰) and their high variability (up to 28.3‰ in FmPy at framboid scale; region S4_2, Fig. 5B, Table 1) might be explained either by Rayleigh distillation processes (Canfield and Teske, 1996; Ohmoto and Goldhaber, 1997; Drake et al., 2015; Jørgensen et al., 2019) in confined environments or by sulphate-driven anaerobic oxidation of methane in sulphate–methane transition zones, according to the model developed by, among others, Jørgensen et al. (2004), Borowski et al. (2013), Deusner et al. (2014), and especially by Lin et al. (2016b), Lin et al. (2017) from the analysis of sedimentary columns in regions with upward methane fluxes.

In our work, the three regions in which mapping and isotopic analysis were conducted (Fig. 5) correspond to two framboids from the same hand sample. They are, indeed, results from a single Luarca Fm. sample. The lack of data from strata above and below the level of the studied sample does not allow an unequivocal decision on a dissimilatory sulphate reduction + Rayleigh distillation model or on a S-AOM model. As far as we know, $\delta^{34}S$ variability at the framboid scale such as those presented in our work, attributed to Rayleigh distillation processes, have not been reported in natural environments. However, $\delta^{34}S$ variability which is even greater in a single pyrite crystal was reported in a borehole core (Drake et al., 2015). As for the S-AOM model, although the succession of phases of pyrite precipitation substantially agrees with that proposed by Lin et al. (2016b), adopting that model assumes that the framboidal nuclei with heavier $\delta^{34}S$ form in the sulphate–methane transition zone. On the other hand, in our samples, we have not found the pyrite tubes and bars related to the upward methane fluxes described by Lin et al. (2016b), Lin et al. (2016a) and Zhang et al. (2014).

Mean $\delta^{34}S$ values in the OgPy and ShPy types are +20.5‰ and +19.7‰, with standard deviations of 2.3 and 1.5, respectively (Table 2). These $\delta^{34}S$ values are slightly lighter than those of Ordovician marine

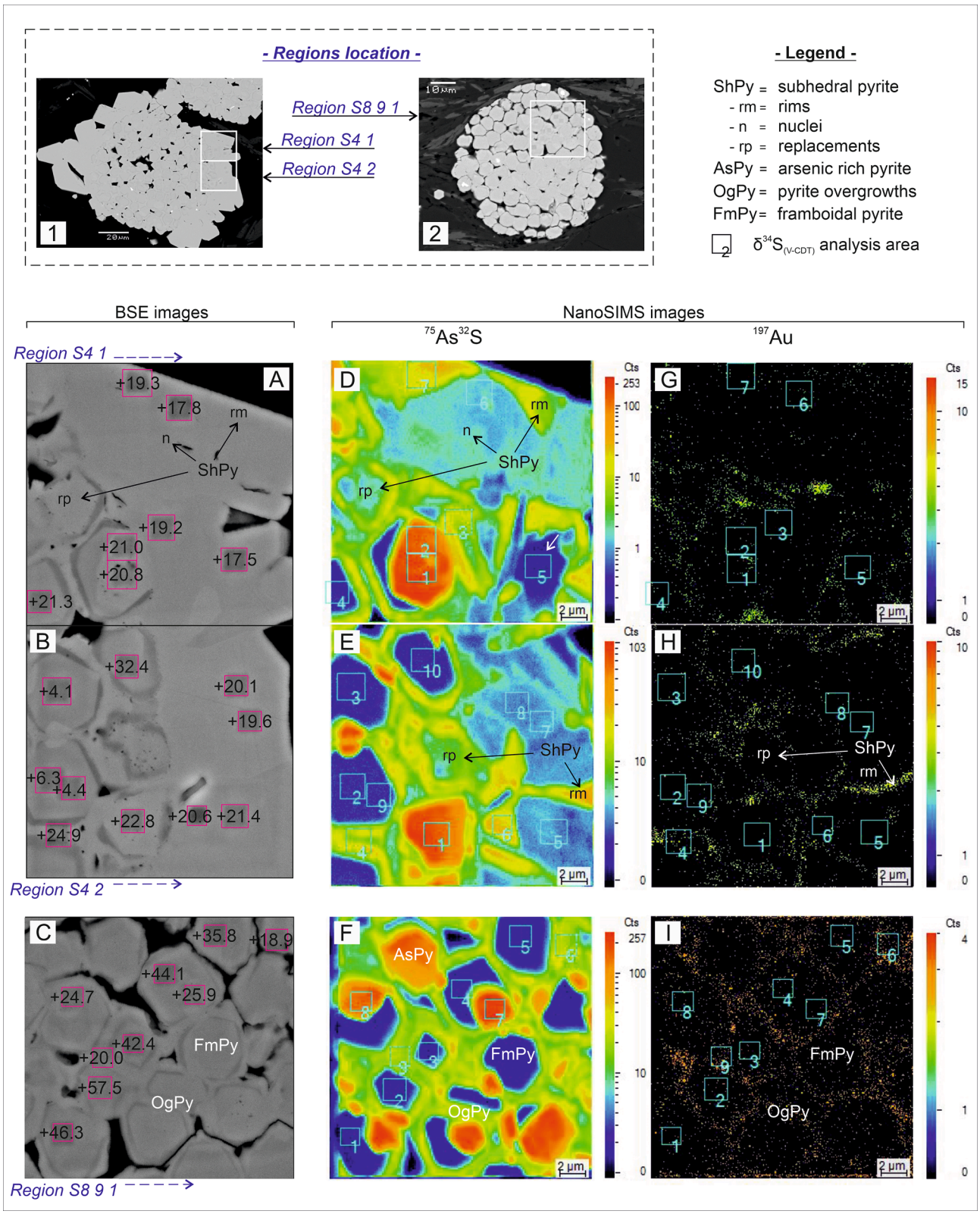

Fig. 5. BSE and NanoSIMS images of the areas that were mapped and subjected to isotopic analysis. 1 and 2) BSE images showing the spatial position of the three regions represented in the rest of the images. A, B and C) BSE images of the 3 mapped regions. D, E and F) NanoSIMS maps of $^{75}As^{32}S$ distribution. G, H and I) NanoSIMS maps of ^{197}Au distribution. In BSE images (A to C), $\delta^{34}S_{(‰\ V\text{-}CDT)}$ results have been placed over the depressions generated by the analytical process. The different images in the same row correspond to the same region.

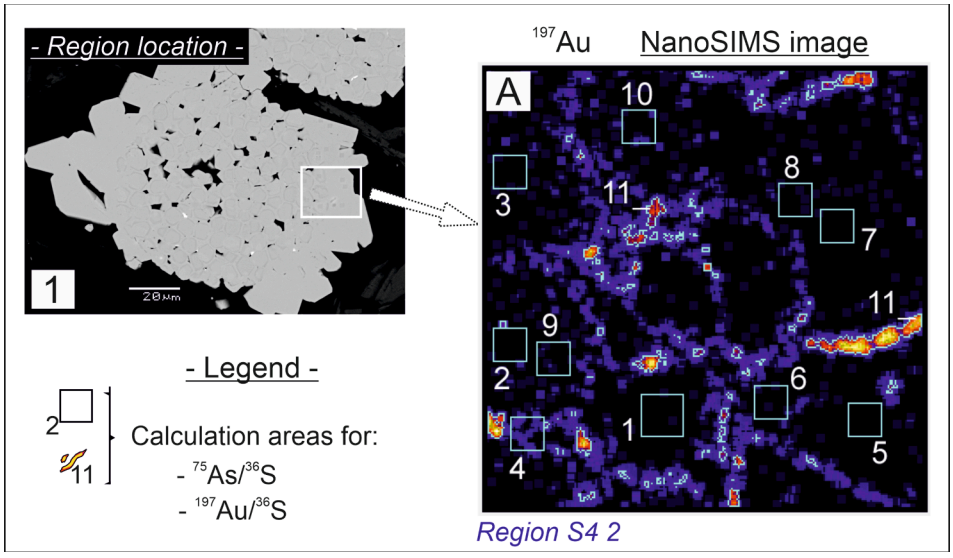

Fig. 6. Location of the 11 areas in which As, Au and S isotopic ratios were quantified by NanoSIMS.

Table 1
$\delta^{34}S$ data and As, Au and S isotopic ratios analysed by NanoSIMS.

Region	Analysis	Pyrite Type	$^{75}As/^{36}S$	$^{197}Au/^{36}S$	$\delta^{34}S$ (‰, V-CDT)	2σ
S8_9_1	1	Framboidal			+46.3	*0.6*
	2	Framboidal			+57.5	*0.6*
	3	Framboidal			+42.4	*0.6*
	4	Framboidal			+44.1	*0.6*
	5	Framboidal			+35.8	*0.6*
	6	Overgrowth			+18.9	*0.6*
	7	Arsenic-rich			+25.9	*0.6*
	8	Arsenic-rich			+24.7	*0.6*
	9	Overgrowth			+20.0	*0.6*
S4_1	1	Arsenic-rich			+20.8	*0.6*
	2	Arsenic-rich			+21.0	*0.6*
	3	Overgrowth			+19.2	*0.6*
	4	Framboidal			+21.3	*0.6*
	5	Framboidal			+17.5	*0.6*
	6	Subhedral			+17.8	*0.6*
	7	Overgrowth			+19.3	*0.6*
S4_2	1	Arsenic-rich	0.356	1.45E-05	+22.8	*0.6*
	2	Framboidal	0.006	0.00E+00	+6.3	*0.6*
	3	Framboidal	0.005	5.38E-05	+4.1	*0.6*
	4	Overgrowth	0.070	5.97E-04	+24.9	*0.6*
	5	Subhedral	0.013	0.00E+00	+21.4	*0.6*
	6	Overgrowth	0.099	9.49E-05	+20.6	*0.6*
	7	Subhedral	0.013	0.00E+00	+19.6	*0.6*
	8	Subhedral	0.010	9.08E-05	+20.1	*0.6*
	9	Framboidal	0.005	9.28E-05	+4.4	*0.6*
	10	Framboidal	0.005	1.88E-04	+32.4	*0.6*
	11		0.052	3.85E-03		

σ = standard deviation.

sulphate, which present low variability, especially when compared to the $\delta^{34}S$ data from FmPy (Fig. 7C). Geological literature indicates that when H_2S concentration decreases, the growth of framboids stops, and pyrite overgrowths may form over the framboids (e.g., Sawlowicz, 1993; Ohfuji and Rickard, 2005; Wei et al., 2012; Ding et al., 2014; Lin et al., 2016b; Gregory et al., 2019). On the other hand, euhedral pyrite precipitates directly in a less saturated pore water environment (e.g., Ohfuji and Rickard, 2005; Taylor and Macquaker, 2011; Lin et al., 2016b), usually at the end of the early diagenesis (Coleman and Raiswell, 1995; Taylor and Macquaker, 2000; Roychoudhury et al., 2003). In the case where the paradigm is the model of Lin et al. (2016b), this data from OgPy and ShPy is compatible with deposition under the sulphate–-methane transition zone.

AsPy is the type of pyrite with highest As content among those described in this work. Its $\delta^{34}S$ values are slightly heavier than in OgPy and ShPy and, like these, show little variability (Table 2). The succession of framboidal pyrites, overgrowths and subhedral pyrites has been frequently described in diagenetic environments (e.g., Sawlowicz, 1993; Wei et al., 2012; Ding et al., 2014; Lin et al., 2016b). On the contrary, the replacement of diagenetic pyrites by As-rich pyrite nodules (AsPy), and with no detectable Au in NanoSIMS analyses, has not been described in the literature as far as we know. The proximity of AsPy to the other members of the observed transition from framboidal to subhedral suggests the AsPy precipitation took place during diagenesis.

Regarding ShPy, its As content (Fig. 5) and its relationship with the tectonic foliation (Fig. 2E–F) evidence the existence of different growth phases. Even though ShPy usually appears within S_1, occasionally S_1 is cut by outer areas of ShPy crystals (yellow arrows in Fig. 2F). Consequently, although ShPy formed mainly in a diagenetic environment, the last phase of ShPy growth would most likely have occurred in a metamorphic environment, on an aggregation model, with overgrowth of metamorphic pyrites over diagenetic pyrites (Scott et al., 2009).

5.3. Au, As and S source, release and its relation with OGDs

The $\delta^{34}S$ isotopic signature in all the types of pyrite analysed in this study (Table 2) is coherent with a source of Ordovician marine sulphate, in which the involvement of lighter magmatic sulphur is not required, despite the presence of volcanic rocks interstratified among Luarca Fm. shale layers (González-Menéndez et al., 2021). According to the model by Large et al. (2011), the gold, arsenic and other trace elements are introduced into the sedimentary basin by stream water. Bacteria might have played a significant role in Au extraction from seawater (Zhang et al., 1997), linking metals to organic compounds in the black muds (e.g., Calvert and Pedersen, 1993; Zhang et al., 1995; Helz et al., 1996; Nekrasov, 1996; Wood, 1996; Tribovillard et al., 2006; Shpirt et al., 2007). These studies of the geochemistry of trace elements associated with Au complexed in organic material in recent oxic/anoxic marine sediments combine with the framboidal pyrite growth model observed in cores from the sulphate–methane transition zone (Lin et al., 2016a, 2016b; Zhang et al., 2014) to provide insight into current processes. During diagenesis As and Au are transferred from the organic matter to

Table 2
$\delta^{34}S$ data in different types of pyrite from Luarca Fm. and sulphides from OGDs.

	Luarca Fm. Shales NanoSIMS Data					Volcanic rocks	OGDs
Sulphide	FmPy	OgPy	AsPy	ShPy	Sin-kinematic Py (*)	Py (*)	Apy,Py,Sph (**)
n=	11	6	5	4	9	2	17
Maximum	+57.5	+24.9	+25.9	+21.4	+28.4	+7.8	+23.1
Minimum	+4.1	+18.9	+20.8	+17.8	+2.1	+7.6	+8.0
Mean	+28.4	+20.5	+23.0	+19.7	+14.4	+7.7	+12.4
σ	*18.7*	*2.3*	*2.2*	*1.5*	*9.6*	*0.1*	*3.8*

n = number of analyses; σ = standard deviation; Apy = arsenopyrite, Py = pyrite, Sph = sphalerite; (*) Gómez-Fernández et al. (2019), (**) Gómez-Fernández et al. (2012).

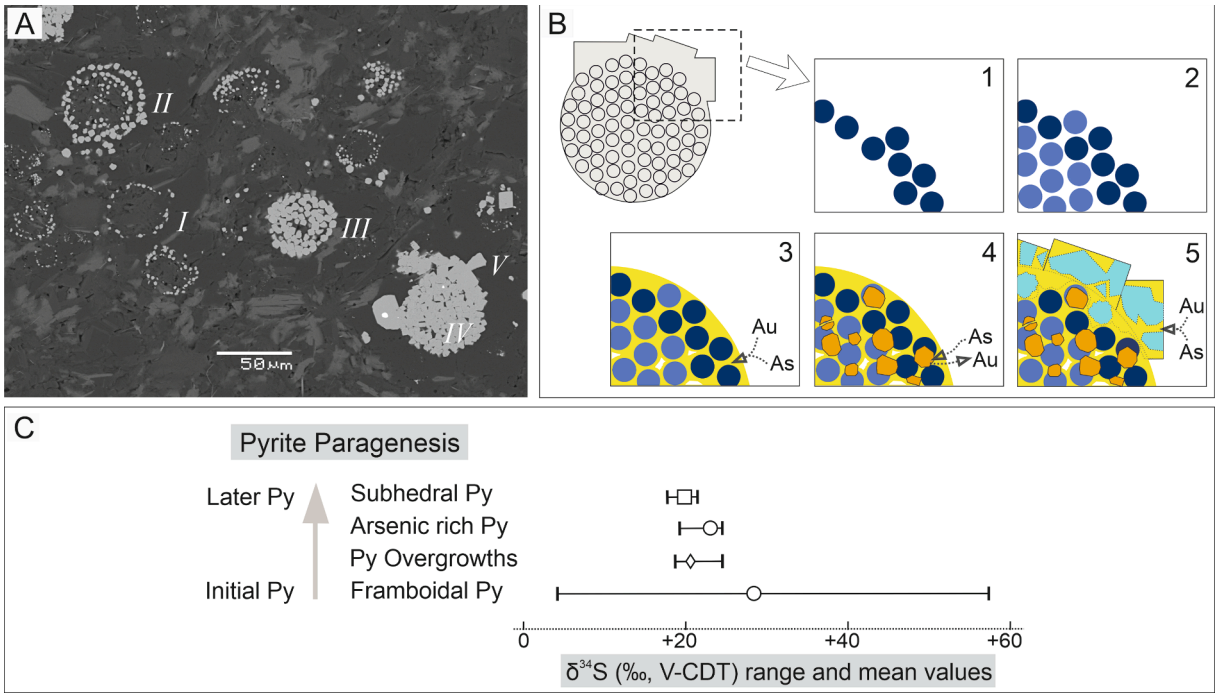

Fig. 7. Representation of the polyphasic growth of pyrite. A) BSE image showing pyrites in different growth stages: *I* to *III*) progressive development of framboids; *IV*) overgrowths; *V*) subhedral. B) Diagram of growth process: 1) nucleation of FmPy crystals, preferentially in the outer part of the framboid (dark blue); 2) FmPy nucleation continues, preferentially inside the framboid, with heavier sulphur (blue); 3) OgPy development (yellow); 4) growth of As-rich (orange) pyrite nodules (AsPy); (5) ShPy development, with nuclei (light blue), rims (yellow) and FmPy replacements (light blue). C) Paragenetic diagram and $\delta^{34}S$ range and mean values of the different phases of pyrite.

the growing pyrite (Large et al., 2011), which would explain their presence in OgPy.

Given that the sin-kinematic pyrite is dominant in the Luarca Fm., the $\delta^{34}S$ isotopic signature of the set of pyrites from this formation will be similar to that of sulphur from sulphides in OGDs (Table 2). In addition, the replacement of previous pyrites by AsPy could release Au to the system, which will later deposit in ShPy rims and even in OGDs in the district (Gómez-Fernández et al., 2012; Cunningham et al., 2019). Therefore, the hypothesis of Gómez-Fernández et al. (2019), proposing that the source of Au in OGDs was in the Luarca Fm. black shales, while not excluding other possible sources, merits further consideration.

5.4. Comparison with previous NanoSIMS studies on pyrites

NanoSIMS has been applied to various forms of pyrites in genetic studies on gold deposits (e.g., Barker et al., 2009; Yan et al., 2018; Li et al., 2019; Liang et al., 2019, 2020; Zhao et al., 2020). Application of NanoSIMS to the characterization of framboidal pyrites is still uncommon, and only a few researchers have employed this technique to obtain: (1) metals, S and As isotopic mappings in pyrites, most of the time related to Carlin-style and orogenic gold deposits (Zhao et al., 2018; Liang et al., 2019; Gregory et al., 2019; Wu et al., 2020), (2) C and N mappings (Wacey et al., 2015; Gregory et al., 2019; Wu et al., 2020), related to distribution of organic matter in sedimentary/diagenetic environments, (3) C, S, Fe and Al mappings (Peng et al., 2017), related to the formation of carbonate pipes in sedimentary environments with anaerobic oxidation of methane and (4) analysis of $\delta^{34}S$ of pyrite types displayed in maps (Wacey et al., 2015; Peng et al., 2017; Zhao et al., 2018; Liang et al., 2019; Zuo et al., 2021), which contribute genetical data about sediments and ore deposits.

None of the referenced works shows mapping with geochemical contrasts significant enough to allow discrimination between what we refer to as FmPy and OgPy, although they often report granulated structures within framboids, which suggests the presence of nuclei and overgrowths. On the other hand, in Zhao et al. (2018), Gregory et al. (2019) and Wu et al. (2020) overgrowths of pyrite over the outer surface of the whole framboid are shown. None of these works deals with similar phases to AsPy described in this paper. However, they do show sub to euhedral pyrite, formed by growth over previous pyrites (Wacey et al., 2015; Gregory et al., 2019) or by recrystallization of the latter (Zhao

et al., 2018).

Regarding $\delta^{34}S$, a key factor to be considered in studies at nanoscale is the size of the framboids and of their inner structures. Luarca Fm. framboids, studied in the present paper, reach 75 μm in size (framboid of the S4_1 and _2 regions, Fig. 5), significantly larger than those from framboids described in Wacey et al. (2015), Peng et al. (2017), Zhao et al. (2018), Liang et al. (2019) and Zuo et al. (2021). FmPy nuclei described in the present work frequently reach 5 μm in size, with the implication that areas for $\delta^{34}S$ analyses did not exceed the perimeter of the nuclei, allowing isotopic characterization of single nuclei, which to our knowledge has not been done before. The same applies for OgPy, AsPy and ShPy, which are also large enough to be analyzed without contamination from other surrounding pyrite types.

In Zuo et al. (2021), a model showing growth from the center outwards is proposed for framboids. Gregory et al. (2019), however, proposed two growth models for pyrite in nodules; pervasive growth and concentric growth. None of these three models fits the processes observed in our research. In this paper, the first FmPy nuclei to form group in the periphery of framboids (Fig. 3A and 7A) and then start to form in the central region until completion of the framboidal structure.

For our study, NanoSIMS images allowed the observation of AsPy nodules, hidden to SEM. They are evidence of a succession of phases of pyrite precipitation (Figs. 4 and 5), rather than recrystallizations, two of which imply replacement of previous pyrites. To a great extent, the sequence of pyrite precipitation could be determined, as well as the processes and the diagenetic/metamorphic environments in which pyrite precipitation took place.

6. Conclusions

Four types of pyrites (framboidal -FmPy-, overgrowth -OgPy-, subhedral -ShPy- and As-rich -AsPy-) were identified by NanoSIMS mapping. They correspond to different phases of pyrite precipitation/replacement in a diagenetic environment. However, the growth of ShPy would have followed an aggregation model, in which the last phase of growth takes place in a metamorphic environment. The first three types of pyrite have been frequently described in the geological literature as formed in pore water in black muds (e.g., Lin et al., 2016b). However, the existence of nodular As-rich pyrites (AsPy) replacing previous pyrites, has not been described from geological contexts similar to the context studied in this work, as far as we know.

Framboids studied in the present work reach 75 μm in size, significantly larger than those described in most previous NanoSIMS studies. They are large enough to permit analysis of $\delta^{34}S$ without contamination from edge effects with different surrounding pyrite types. This allowed isotopic characterization to be performed on single framboid microcrystals.

The isotopic signature of the sulphur involved in the precipitation of the analysed pyrites is in good agreement with the hypothesis of an Ordovician marine source of sulphur.

Two distinct phases of Au precipitation were observed, associated with OgPy and ShPy respectively. Replacement of OgPy by AsPy would have resulted in the release of Au to the system from Luarca Fm. pyrites, unlike the framboidal to euhedral recrystallization process observed in other gold districts (e.g., Large et al., 2011; Zhao et al., 2018; Wu et al., 2020). Therefore, the hypothesis proposing that the gold source for OGDs in our district was in the Luarca Fm. shales (Gómez-Fernández et al., 2019) is supported by the results of the present research. However, other possible sources are not excluded.

Declaration of Competing Interest

The authors declare that they have no known competing financial interests or personal relationships that could have appeared to influence the work reported in this paper.

Acknowledgements

This project was funded by Project 0284_ESMIMET_3_E (INTERREG V-A Spain-Portugal Cooperation Programme, 2014-20) and by Project LE167G18 (Junta de Castilla y León, Spain). Authors are grateful to Ian A. Franchi and Xuchao Zhao (Planetary and Space Sciences, The Open University, Milton Keynes, UK), Clemente Recio (University of Salamanca, Spain), Emilio J. González Clavijo (Spanish Geological Survey, IGME; Salamanca, Spain) and Will Brownscombe (Natural History Museum, London, UK).

References

Barker, S.L.L., Hickey, K.A., Cline, J.S., Dipple, G.M., Kilburn, M.R., Vaughan, J.R., Longo, A.A., 2009. Uncloaking invisible gold: use of NanoSIMS to evaluate gold, trace elements, and sulfur isotopes in pyrite from Carlin-type gold deposits. Econ. Geol. 104 (7), 897–904. https://doi.org/10.2113/econgeo.104.7.897.

Barros Lorenzo, J.C., 1989. New geological and cartographic data about the south limb of the Truchas Synclinorium (Ourense-León), NW Spain. Cadernos Laboratorio Xeológico de Laxe 14, 93–116.

Bierlein, F.P., Cartwright, I., McKnight, S., 2001. The role of carbonaceous 'indicator' slates in the genesis of lode gold mineralization in the Western Lachlan Orogen, Victoria, Southeastern Australia. Econ. Geol. 96 (3), 431–451. https://doi.org/10.2113/gsecongeo.96.3.431.

Boetius, A., Ravenschlag, K., Schubert, C.J., Rickert, D., Widdel, F., Gieseke, A., Amann, R., Jørgensen, B.B., Witte, U., Pfannkuche, O., 2000. A marine microbial consortium apparently mediating anaerobic oxidation of methane. Nature 407 (6804), 623–626. https://doi.org/10.1038/35036572.

Borowski, W.S., Rodriguez, N.M., Paull, C.K., Ussler, W., 2013. Are ^{34}S-enriched authigenic sulfide minerals a proxy for elevated methane flux and gas hydrates in the geologic record? Mar. Pet. Geol. 43, 381–395. https://doi.org/10.1016/j.marpetgeo.2012.12.009.

Böttcher, M.E., Smock, A., Cypionka, H., 1998. Sulfur isotope fractionation during experimental precipitation of iron(II) and manganese(II) sulfide at room temperature. Chem. Geol. 146 (3–4), 127–134. https://doi.org/10.1016/S0009-2541(98)00004-7.

Böttcher, M.E., Thamdrup, B., 2001. Oxygen and sulfur isotope fractionation during anaerobic bacterial disproportionation of elemental sulfur. Geochim. Cosmochim. Acta 65 (10), 1601–1609. https://doi.org/10.1016/S0016-7037(00)00628-1.

Brüchert, V., Knoblauch, C., Jørgensen, B.B., 2001. Controls on stable sulfur isotope fractionation during bacterial sulfate reduction in arctic sediments. Geochim. Cosmochim. Acta 65 (5), 763–776. https://doi.org/10.1016/S0016-7037(00)00557-3.

Brunner, B., Bernasconi, S.M., 2005. A revised isotope fractionation model for dissimilatory sulfate reduction in sulfate reducing bacteria. Geochim. Cosmochim. Acta 69 (20), 4759–4771. https://doi.org/10.1016/j.gca.2005.04.015.

Calvert, S.E., Pedersen, T.F., 1993. Geochemistry of recent oxic and anoxic marine sediments: Implications for the geological record. Mar. Geol. 113 (1-2), 67–88. https://doi.org/10.1016/0025-3227(93)90150-T.

Canfield, D.E., Farquhar, J., Zerkle, A.L., 2010. High isotope fractionations during sulfate reduction in a low-sulfate euxinic ocean analog. Geology 38 (5), 415–418. https://doi.org/10.1130/G30723.

Canfield, D.E., Teske, A., 1996. Late Proterozoic rise in atmospheric oxygen concentration inferred from phylogenetic and sulphur-isotope studies. Nature 382 (6587), 127–132. https://doi.org/10.1038/382127a0.

Canfield, D., Thamdrup, B., 1994. The production of ^{34}S-depleted sulfide during bacterial disproportionation of elemental sulfur. Science 266 (5193), 1973–1975. https://doi.org/10.1126/science:11540246.

Cárdenes, V., Merinero, R., de Boever, W., Rubio-Ordóñez, A., Dewanckele, J., Cnudde, J. P., Boone, M., Van Hoorebeke, L., Cnudde, V., 2016. Characterization of micropyrite populations in low-grade metamorphic slate: a study using high-resolution X-ray tomography. Palaeogeogr. Palaeoclimatol. Palaeoecol. 441, 924–935. https://doi.org/10.1016/j.palaeo.2015.10.044.

Cárdenes, V., Rubio-Ordóñez, A., Wichert, J., Cnudde, J.P., Cnudde, V., 2014. Petrography of roofing slates. Earth Sci. Rev. 138, 435–453. https://doi.org/10.1016/j.earscirev.2014.07.003.

Claypool, G.E., Holser, W.T., Kaplan, I.R., Sakai, H., Zak, I., 1980. The age curves of sulfur and oxygen isotopes in marine sulfate and their mutual interpretation. Chem. Geol. 28 (C), 199–260. https://doi.org/10.1016/0009-2541(80)90047-9.

Coleman, M.L., Raiswell, R., 1995. Source of carbonate and origin of zonation in pyritiferous carbonate concretions: evaluation of a dynamic model. Am. J. Sci. 295 (3), 282–308. https://doi.org/10.2475/ajs.295.3.282.

Coveney, R.M., Nansheng, C., 1991. Ni-Mo-PGE-Au-rich ores in Chinese black shales and speculations on possible analogues in the United States. Miner. Deposita 26 (2), 83–88. https://doi.org/10.1007/BF00195253.

Cunningham, J.K., Gómez-Fernández, F., González-Menéndez, L., Beard, A.D., 2019. Welsh and Spanish orogenic gold – a comparative study, in: Life with Ore Deposits on Earth – 15th SGA Biennial Meeting 2019, Glasgow, Volume 2, pp. 733–735.

Deusner, C., Holler, T., Arnold, G.L., Bernasconi, S.M., Formolo, M.J., Brunner, B., 2014. Sulfur and oxygen isotope fractionation during sulfate reduction coupled to anaerobic oxidation of methane is dependent on methane concentration. Earth Planet. Sci. Lett. 399, 61–73. https://doi.org/10.1016/j.epsl.2014.04.047.

Ding, H., Yao, S., Chen, J., 2014. Authigenic pyrite formation and re-oxidation as an indicator of an unsteady-state redox sedimentary environment: evidence from the intertidal mangrove sediments of Hainan Island, China. Cont. Shelf Res. 78, 85–99. https://doi.org/10.1016/j.csr.2014.02.011.

Donald, R., Southam, G., 1999. Low temperature anaerobic bacterial diagenesis of ferrous monosulfide to pyrite. Geochim. Cosmochim. Acta 63 (13–14), 2019–2023. https://doi.org/10.1016/S0016-7037(99)00140-4.

Drake, H., Tullborg, E.L., Whitehouse, M., Sandberg, B., Blomfeldt, T., Åström, M.E., 2015. Extreme fractionation and micro-scale variation of sulphur isotopes during bacterial sulphate reduction in deep groundwater systems. Geochim. Cosmochim. Acta 161, 1–18. https://doi.org/10.1016/j.gca.2015.04.014.

Goldfarb, R.J., Groves, D.I., 2015. Orogenic gold: Common or evolving fluid and metal sources through time. Lithos 233, 2–26. https://doi.org/10.1016/j.lithos.2015.07.011.

Gómez-Fernández, F., Castaño, M.A., Bauluz, B., Ward, C.R., 2009a. Optical microscope and SEM evaluation of roofing slate fissility and durability. Mater. Constr. 59 (296), 91–104. https://doi.org/10.3989/mc.2009.44007.

Gómez-Fernández, F., Cunningham, J.K., Caldevilla, P., Herrero-Hernández, A., Beard, A. D., 2019. The source of Au and S of the orogenic gold deposits in the Llamas de Cabrera district (Iberian Variscan Massif), in: Life with Ore Deposits on Earth – 15th SGA Biennial Meeting 2019, Glasgow, Volume 2, pp. 842–845.

Gómez-Fernández, F., Ramajo, B., Roces, L., Castañón, A.M., Guerrero, A.M., 2017. Splitting of roofing slates: analysis of the process based on SEM, TMA, TG/DSC, and XRD. J. Mater. Civ. Eng. 29 (9), 04017094. https://doi.org/10.1061/(asce)mt.1943-5533.0001936.

Gómez-Fernández, F., Vindel, E., Martín-Crespo, T., Sánchez, V., González Clavijo, E., Matías, R., 2012. The Llamas de Cabrera gold district, a new discovery in the Variscan basement of northwest Spain: a fluid inclusion and stable isotope study. Ore Geol. Rev. 46, 68–82. https://doi.org/10.1016/j.oregeorev.2012.02.001.

Gómez-Fernández, F., Ward, C.R., Bauluz, B., 2009b. XRD, electron microscopy (EMPA, SEM, TEM) and XRF characterization of roofing slates from NW Spain. Cadernos do Laboratorio Xeoloxico de Laxe 34, 127–142.

González-Menéndez, L., Gómez-Fernández, F., Cunningham, J.K., Menéndez, S., Caldevilla, P., Gallastegui, G., 2021. Ordovician volcanic rocks record rifting, metasomatism, metamorphism and hydrothermal-gold mineralization processes (Variscan Truchas Syncline, NW Iberia, Spain). J. Iberian Geol., doi.org/10.1007/s41513-020-00147-8.

Gregory, D.D., Large, R.R., Halpin, J.A., Baturina, E.L., Lyons, T.W., Wu, S., Danyushevsky, L., Sack, P.J., Chappaz, A., Maslennikov, V.V., Bull, S.W., 2015. Trace element content of sedimentary pyrite in black shales. Econ. Geol. 110 (6), 1389–1410. https://doi.org/10.2113/econgeo.110.6.1389.

Gregory, D.D., Mukherjee, I., Olson, S.L., Large, R.R., Danyushevsky, L.V., Stepanov, A. S., Avila, J.N., Cliff, J., Ireland, T.R., Raiswell, R., Olin, P.H., Maslennikov, V.V., Lyons, T.W., 2019. The formation mechanisms of sedimentary pyrite nodules determined by trace element and sulfur isotope microanalysis. Geochim. Cosmochim. Acta 259, 53–68. https://doi.org/10.1016/j.gca.2019.05.035.

Groves, D.I., Goldfarb, R.J., Gebre-Mariam, M., Hagemann, S.G., Robert, F., 1998. Orogenic gold deposits: a proposed classification in the context of their crustal distribution and relationship to other gold deposit types. Ore Geol. Rev. 13 (1–5), 7–27. https://doi.org/10.1016/S0169-1368(97)00012-7.

Habicht, K., Canfield, D.E., Rethmeier, J., 1998. Sulfur isotope fractionation during bacterial reduction and disproportionation of thiosulfate and sulfite. Geochim. Cosmochim. Acta 62 (15), 2585–2595. https://doi.org/10.1016/S0016-7037(98)00167-7.

Helz, G.R., Miller, C.V., Charnock, J.M., Mosselmans, J.F.W., Pattrick, R.A.D., Garner, C. D., Vaughan, D.J., 1996. Mechanism of molybdenum removal from the sea and its concentration in black shales: EXAFS evidence. Geochim. Cosmochim. Acta 60 (19), 3631–3642. https://doi.org/10.1016/0016-7037(96)00195-0.

Herail, G., 1984. Géomorfologie et gitologie de l'or détritique. Piédmont et bassins intramontagneux du Nord-Ouest de lEspagne. Centre National de la Recherche Scientifique (CNRS), Paris.

Hinrichs, K.-U., Hayes, J.M., Sylva, S.P., Brewer, P.G., DeLong, E.F., 1999. Methane-consuming archaebacteria in marine sediments. Nature 398 (6730), 802–805. https://doi.org/10.1038/19751.

Huyck, H.L.O., 1990. Proposed definition of "black shale" and "metalliferous black shale" for IGCP #254. In: Book of Abstracts 8th IAGOD Symposium. Geological Survey of Canada, Ottawa, pp. A183–A184.

Jørgensen, B.B., Böttcher, M.E., Lüschen, H., Neretin, L.N., Volkov, I.I., 2004. Anaerobic methane oxidation and a deep H_2S sink generate isotopically heavy sulfides in Black Sea sediments. Geochim. Cosmochim. Acta 68 (9), 2095–2118. https://doi.org/10.1016/j.gca.2003.07.017.

Jørgensen, B.B., Findlay, A.J., Pellerin, A., 2019. The biogeochemical sulfur cycle of marine sediments. Front. Microbiol. 10, 849. https://doi.org/10.3389/fmicb.2019.00849.

Ketris, M.P., Yudovich, Y.E., 2009. Estimations of Clarkes for Carbonaceous biolithes: World averages for trace element contents in black shales and coals. Int. J. Coal Geol. 78 (2), 135–148. https://doi.org/10.1016/j.coal.2009.01.002.

Knittel, K., Boetius, A., 2009. Anaerobic oxidation of methane: progress with an unknown process. Annu. Rev. Microbiol. 63 (1), 311–334. https://doi.org/10.1146/annurev.micro.61.080706.093130.

Large, R.R., Bull, S.W., Maslennikov, V.V., 2011. A carbonaceous sedimentary source rock model for Carlin-type and orogenic gold deposits. Econ. Geol. 106 (3), 331–358. https://doi.org/10.2113/econgeo.106.3.331.

Large, R.R., Maslennikov, V., Robert, F., Danyushevsky, L.V., Chang, Z., 2007. Multistage sedimentary and metamorphic origin of pyrite and gold in the giant Sukhoi Log deposit, Lena gold province, Russia. Econ. Geol. 102 (7), 1233–1267. https://doi.org/10.2113/gsecongeo.102.7.1233.

Large, R.R., Thomas, H., Craw, D., Henne, A., Henderson, S., 2012. Diagenetic pyrite as a source for metals in orogenic gold deposits, Otago Schist, New Zealand. N. Z. J. Geol. Geophys. 55 (2), 137–149. https://doi.org/10.1080/00288306.2012.682282.

Li, J., Hu, R., Zhao, C., Zhu, J., Huang, Y., Gao, W., Li, J., Zhuo, Y., 2019. Sulfur isotope and trace element compositions of pyrite determined by NanoSIMS and LA-ICP-MS: new constraints on the genesis of the Shuiyindong Carlin-like gold deposit in SW China. Miner. Deposita 55 (7), 1279–1298. https://doi.org/10.1007/s00126-019-00929-w.

Liang, J., Li, J., Liu, X., Zhai, W., Huang, Y.i., Zhao, J., Sun, W., Song, M., Li, J., 2020. Multiple element mapping and in-situ S isotopes of Au-carrying pyrite of Shuiyindong gold deposit, southwestern China using NanoSIMS: constraints on Au sources, ore fluids, and mineralization processes. Ore Geol. Rev. 123, 103576. https://doi.org/10.1016/j.oregeorev.2020.103576.

Liang, J., Li, J., Sun, W., Zhao, J., Zhai, W., Huang, Y., Song, M., Ni, S., Xiang, Q., Zhang, J., Hao, J., Nan, Z., Li, J., 2019. Source of ore-forming fluids of the Yangshan gold field, western Qinling orogen, China: evidence from microthermometry, noble gas isotopes and in situ sulfur isotopes of Au-carrying pyrite. Ore Geol. Rev. 105, 404–422. https://doi.org/10.1016/j.oregeorev.2018.12.029.

Lin, Q., Wang, J., Taladay, K., Lu, H., Hue, G., Sun, F., Lin, R., 2016a. Coupled pyrite concentration and sulfur isotopic insight into the paleo sulfate–methane transition zone (SMTZ) in the northern South China Sea. J. Asian Earth Sci. 115, 547–556. https://doi.org/10.1016/j.jseaes.2015.11.001.

Lin, Z., Sun, X., Peckmann, J., Lu, Y., Xu, L., Strauss, H., Zhou, H., Gong, J., Lu, H., Teichert, B.M.A., 2016b. How sulfate-driven anaerobic oxidation of methane affects the sulfur isotopic composition of pyrite: A SIMS study from the South China Sea. Chem. Geol. 440, 26–41. https://doi.org/10.1016/j.chemgeo.2016.07.007.

Lin, Z., Sun, X., Strauss, H., Lu, Y., Gong, J., Xu, L., Lu, H., Teichert, B.M.A., Peckmann, J., 2017. Multiple sulfur isotope constraints on sulfate-driven anaerobic oxidation of methane: Evidence from authigenic pyrite in seepage areas of the South China Sea. Geochim. Cosmochim. Acta 211, 153–173. https://doi.org/10.1016/j.gca.2017.05.015.

Loukola-Ruskeeniemi, K., Lahtinen, H., 2013. Multiphase evolution in the black-shale-hosted Ni–Cu–Zn–Co deposit at Talvivaara, Finland. Ore Geol. Rev. 52, 85–99. https://doi.org/10.1016/j.oregeorev.2012.10.006.

Lyons, T.W., 1997. Sulfur isotopic trends and pathways of iron sulfide formation in upper Holocene sediments of the anoxic Black Sea. Geochim. Cosmochim. Acta 61 (16), 3367–3382. https://doi.org/10.1016/S0016-7037(97)00174-9.

Magnall, J.M., Gleeson, S.A., Stern, R.A., Newton, R.J., Poulton, S.W., Paradis, S., 2016. Open system sulphate reduction in a diagenetic environment – isotopic analysis of barite ($\delta^{34}S$ and $\delta^{18}O$) and pyrite ($\delta^{34}S$) from the Tom and Jason Late Devonian Zn-Pb-Ba deposits, Selwyn Basin, Canada. Geochim. Cosmochim. Acta 180, 146–163. https://doi.org/10.1016/j.gca.2016.02.015.

Marcos, A., 1973. Las series del Paleozoico Inferior y la estructura herciniana del occidente de Asturias (NW de España). Trabajos de Geología de la Universidad de Oviedo 6, 1–113. https://doi.org/10.17811/tdg.6.1973.3-113.

Mason, J.S., Bevins, R.E., Alderton, D.H.M., 2002. Ore Mineralogy of the mesothermal gold lodes of the Dolgellau Gold Belt, North Wales. Trans. Instit. Min. Metall. (Section B, Applied earth science) 111 (3), 203–214. https://doi.org/10.1179/037174502765188600.

Matías, R., Gómez-Fernández, F., 2003. La mina de oro romana de Llamas de Cabrera (León-España), in: Mata-Perelló J.M. (Ed.), Actas del IV Congreso Internacional sobre Patrimonio Geológico y Minero, Utrillas (Teruel), pp. 383–398.

Nekrasov, I.Y., 1996. Geochemistry, Mineralogy and Genesis of Gold Deposits. A.A Balkema, Rotterdam.

Ohfuji, H., Rickard, D., 2005. Experimental syntheses of framboids – a review. Earth Sci. Rev. 71 (3–4), 147–170. https://doi.org/10.1016/j.earscirev.2005.02.001.

Ohmoto, H., Goldhaber, M.B., 1997. Sulfur and carbon isotopes. In: Barnes, H. (Ed.), Geochemistry of Hydrothermal Ore Deposits. Wiley, New York, pp. 517–612.

Pancost, R.D., Sinninghe Damsté, J.S., de Lint, S., van der Maarel, M.J.E.C., Gottschal, J. C., 2000. Biomarker evidence for widespread anaerobic methane oxidation in Mediterranean sediments by a consortium of methanogenic archaea and bacteria. Appl. Environ. Microbiol. 66 (3), 1126–1132. https://doi.org/10.1128/AEM.66.3.1126-1132.2000.

Parviainen, A., Loukola-Ruskeeniemi, K., 2019. Environmental impact of mineralised black shales. Earth Sci. Rev. 192, 65–90. https://doi.org/10.1016/j.earscirev.2019.01.017.

Peng, X., Guo, Z., Chen, S., Sun, Z., Xu, H., Ta, K., Zhang, J., Zhang, L., Li, J., Du, M., 2017. Formation of carbonate pipes in the northern Okinawa Trough linked to strong sulfate exhaustion and iron supply. Geochim. Cosmochim. Acta 205, 1–13. https://doi.org/10.1016/j.gca.2017.02.010.

Pérez-Estaún, A., 1978. La estratigrafía y la estructura de la rama Sur de la Zona Asturoccidental-Leonesa. Memoria del Instituto Geológico y Minero de España 92, Madrid.

Pitcairn, I.K., Teagle, D.A.H., Craw, D., Olivo, G.K., Kerrich, R., Brewer, T.S., 2006. Sources of metals and fluids in orogenic gold deposits: Insights from the Otago and Alpine schists, New Zealand. Econ. Geol. 101 (8), 1525–1546. https://doi.org/10.2113/gsecongeo.101.8.1525.

Polgári, M., Hein, J.R., Vigh, T., Szabó-Drubina, M., Fórizs, I., Bíró, L., Müller, A., Tóth, A.L., 2012. Microbial processes and the origin of the Úrkút manganese deposit, Hungary. Ore Geol. Rev. 47, 87–109. https://doi.org/10.1016/J.OREGEOREV.2011.10.001.

Price, F.T., Shieh, Y.N., 1979. Fractionation of sulfur isotopes during laboratory synthesis of pyrite at low temperatures. Chem. Geol. 27 (3), 245–253. https://doi.org/10.1016/0009-2541(79)90042-1.

Raiswell, R., Canfield, D.E., 1998. Sources of iron for pyrite formation in marine sediments. Am. J. Sci. 298 (3), 219–245. https://doi.org/10.2475/ajs.298.3.219.
Reeburgh, W.S., 2007. Oceanic methane biogeochemistry. Chem. Rev. 107 (2), 486–513. https://doi.org/10.1021/cr050362v.
Rickard, D., 2019. Sedimentary pyrite framboid size-frequency distributions: A meta-analysis. Palaeogeogr. Palaeoclimatol. Palaeoecol. 522, 62–75. https://doi.org/10.1016/j.palaeo.2019.03.010.
Robinson, B., Kusakabe, M., 1975. Quantitative preparation of sulphur dioxide for $^{34}S/^{32}S$ analyses from sulphides by combustion with cuprous oxide. Anal. Chem. 47 (7), 1179–1181. https://doi.org/10.1021/ac60357a026.
Roychoudhury, A.N., Kostka, J.E., Van Cappellen, P., 2003. Pyritization: a palaeoenvironmental and redox proxy reevaluated. Estuar. Coast. Shelf Sci. 57 (5-6), 1183–1193. https://doi.org/10.1016/S0272-7714(03)00058-1.
Rudnicki, M.D., Elderfield, H., Spiro, B., 2001. Fractionation of sulfur isotopes during bacterial sulfate reduction in deep ocean sediments at elevated temperatures. Geochim. Cosmochim. Acta 65 (5), 777–789. https://doi.org/10.1016/S0016-7037(00)00579-2.
Sáez, R., Moreno, C., González, F., Almodóvar, G.R., 2011. Black shales and massive sulfide deposits: causal or casual relationships? Insights from Rammelsberg, Tharsis, and Draa Sfar. Miner. Deposita 46 (5-6), 585–614. https://doi.org/10.1007/s00126-010-0311-x.
Sawlowicz, Z., 1993. Pyrite framboids and their development: a new conceptual mechanism. Geol. Rundsch. 82 (1), 148–156. https://doi.org/10.1007/BF00563277.
Scott, R.J., Meffre, S., Woodhead, J., Gilbert, S.E., Berry, R.F., Emsbo, P., 2009. Development of framboidal pyrite during diagenesis, low-grade regional metamorphism, and hydrothermal alteration. Econ. Geol. 104 (8), 1143–1168. https://doi.org/10.2113/gsecongeo.104.8.1143.
Shepherd, T.J., Bottrell, S.H., 1993. Dolgellau Gold-belt, Harlech district, North Wales, in: Pattrick, R.A.D., Polya, D.A. (Eds.), Mineralisation in the British Isles. Chapman and Hall, London, pp. 187–205.
Shpirt, M.Y., Punanova, S.A., Strizhakova, Y.A., 2007. Trace elements in black and oil shales. Solid Fuel Chem. 41 (2), 119–127. https://doi.org/10.3103/S0361521907020115.
Sim, M.S., Ono, S., Donovan, K., Templer, S.P., Bosak, T., 2011. Effect of electron donors on the fractionation of sulfur isotopes by a marine *Desulfovibrio* sp. Geochim. Cosmochim. Acta 75 (15), 4244–4259. https://doi.org/10.1016/j.gca.2011.05.021.
Sim, M.S., Paris, G., Adkins, J.F., Orphan, V.J., Sessions, A.L., 2017. Quantification and isotopic analysis of intracellular sulfur metabolites in the dissimilatory sulfate reduction pathway. Geochim. Cosmochim. Acta 206, 57–72. https://doi.org/10.1016/j.gca.2017.02.024.
Suárez, A., Barba, P., Heredia, N., Rodríguez Fernández, L.R., 1994. Mapa Geológico de la Provincia de León. Escala 1:200.000. Instituto Tecnológico Geominero de España (ITGE).
Taylor, K.G., Macquaker, J.H.S., 2000. Early diagenetic pyrite morphology in a mudstone-dominated succession: the Lower Jurassic Cleveland Ironstone Formation, eastern England. Sed. Geol. 131 (1–2), 77–86. https://doi.org/10.1016/S0037-0738(00)00002-6.
Taylor, K.G., Macquaker, J.H.S., 2011. Iron minerals in marine sediments record chemical environments. Elements 7 (2), 113–118. https://doi.org/10.2113/gselements.7.2.113.
Tomkins, A.G., 2010. Windows of metamorphic sulfur liberation in the crust: Implications for gold deposit genesis. Geochim. Cosmochim. Acta 74 (11), 3246–3259. https://doi.org/10.1016/j.gca.2010.03.003.
Tornos, F., Spiro, B., Shepherd, T.J., Ribera, F., 1997. Sandstone-hosted gold lodes of the southern West Asturian Leonese Zone (NW Spain): the role of depth in the genesis of the mineralization. Chronique de la Recherche Minière 528 (1), 71–86.
Tribovillard, N., Algeo, T.J., Lyons, T., Riboulleau, A., 2006. Trace metals as paleoredox and paleoproductivity proxies: An update. Chem. Geol. 232 (1-2), 12–32. https://doi.org/10.1016/j.chemgeo.2006.02.012.
Voldman, G.G., Toyos, J.M., 2019. Taxonomy, biostratigraphy and biofacies of an upper Ordovician (Katian) conodont fauna from the Casaio Formation, Northwest Spain. Bull. Geosci. 94 (4), 455–478. https://doi.org/10.3140/bull.geosci.1759.
Wacey, D., Kilburn, M.R., Saunders, M., Cliff, J.B., Kong, C., Liu, A.G., Matthews, J.J., Brasier, M.D., 2015. Uncovering framboidal pyrite biogenicity using nano-scale CN_{org} mapping. Geology 43 (1), 27–30. https://doi.org/10.1130/G36048.1.
Ward, C.R., Gómez-Fernández, F., 2004. Quantitative mineralogical analysis of Spanish roofing slates using the Rietveld method and X-ray powder diffraction data. Eur. J. Mineral. 15 (6), 1051–1062. https://doi.org/10.1127/0935-1221/2003/0015-1051.
Wei, H., Chen, D., Wang, J., Yu, H., Tucker, M.E., 2012. Organic accumulation in the lower Chihsia formation (Middle Permian) of South China: constraints from pyrite morphology and multiple geochemical proxies. Palaeogeogr. Palaeoclimatol. Palaeoecol. 353–355, 73–86. https://doi.org/10.1016/j.palaeo.2012.07.005.
Wei, H., Wei, X., Qiu, Z., Song, H., Shi, G., 2016. Redox conditions across the G-L boundary in South China: Evidence from pyrite morphology and sulfur isotopic compositions. Chem. Geol. 440, 1–14. https://doi.org/10.1016/j.chemgeo.2016.07.009.
Wiedenbeck, M., 2012. Challenges and strategies for the calibration of SIMS geochemical analyses. Microanalytical Reference Materials Topical Conference. Colorado School of Mines Golden, May 15-17, Colorado.
Wignall, P.B., 1994. Black Shales. Oxford University Press, New York.
Wilkin, R.T., Barnes, H.L., Brantley, S.L., 1996. The size distribution of framboidal pyrite in modern sediments: an indicator of redox conditions. Geochim. Cosmochim. Acta 60 (20), 3897–3912. https://doi.org/10.1016/0016-7037(96)00209-8.
Wood, S.A., 1996. The role of humic substances in the transport and fixation of metals of economic interest (Au, Pt, Pd, U, V). Ore Geol. Rev. 11 (1-3), 1–31. https://doi.org/10.1016/0169-1368(95)00013-5.
Wortmann, U.G., Bernasconi, S.M., Böttcher, M.E., 2001. Hypersulfidic deep biosphere indicates extreme sulfur isotope fractionation during single-step microbial sulfate reduction. Geology 29 (7), 647–650. https://doi.org/10.1130/0091-7613(2001)029<0647:HDBIES>2.0.CO;2.
Wu, Y.-F., Evans, K., Fisher, L.A., Zhou, M.-F., Hud, S.-Y., Fougerouse, D., Large, R.R., Li, J.-W., 2020. Distribution of trace elements between carbonaceous matter and sulfides in a sediment-hosted orogenic gold system. Geochim. Cosmochim. Acta 276, 345–362. https://doi.org/10.1016/j.gca.2020.03.006.
Yan, J., Hu, R., Liu, S., Lin, Y., Zhang, J., Fu, S., 2018. NanoSIMS element mapping and sulfur isotope analysis of Au-bearing pyrite from Lannigou Carlin-type Au deposit in SW China: new insights into the origin and evolution of Au-bearing fluids. Ore Geol. Rev. 92, 29–41. https://doi.org/10.1016/j.oregeorev.2017.10.015.
Yoshinaga, M.Y., Holler, T., Goldhammer, T., Wegener, G., Pohlman, J.W., Brunner, B., Kuypers, M.M.M., Hinrichs, K.-U., Elvert, M., 2014. Carbon isotope equilibration during sulphate-limited anaerobic oxidation of methane. Nat. Geosci. 7 (3), 190–194. https://doi.org/10.1038/ngeo2069.
Zhang, J., Lin, Y., Yan, J., Li, J., Yang, W., 2017. Simultaneous determination of sulfur isotopes and trace elements in pyrite with a NanoSIMS 50L. Anal. Methods 9 (47), 6653–6661. https://doi.org/10.1039/C7AY01440F.
Zhang, A., Pan, Y., Weng, C., 1995. The organic geochemistry of auriferous black shales, in: Pasava, J., Kribek, B., and Zak, K., (Eds.), Mineral deposits: From their origin to their environmental impacts. Society for Geology Applied to Mineral Deposits, Prague, pp. 829−831.
Zhang, J., Lu, J., Zhai, J., Fan, Y., 1997. Simulating experiments on enrichment of gold by bacteria and their geochemical significance. Chin. J. Geochem. 16 (4), 369–373. https://doi.org/10.1007/BF02870923.
Zhang, M., Konishi, H., Xu, H.F., Sun, X.M., Lu, H.F., Wu, D.D., Wu, N.Y., 2014. Morphology and formation mechanism of pyrite induced by the anaerobic oxidation of methane from the continental slope of the NE South China Sea. J. Asian Earth Sci. 92 (1), 293–301. https://doi.org/10.1016/j.jseaes.2014.05.004.
Zhao, J., Liang, J., Li, J., Huang, Y., Liu, X., Zhang, J., Hao, J., Sun, W., Li, J., Xie, J., 2020. Gold and sulfur sources of the Taipingdong Carlin-type gold deposit: Constraints from simultaneous determination of sulfur isotopes and trace elements in pyrite using nanoscale secondary ion mass spectroscopy. Ore Geol. Rev. 117 (1), 103299 https://doi.org/10.1016/j.oregeorev.2019.103299.
Zhao, J., Liang, J., Long, X., Li, J., Xiang, Q., Zhang, J., Hao, J., 2018. Genesis and evolution of framboidal pyrite and its implications for the ore-forming process of Carlin-style gold deposits, Southwestern China. Ore Geol. Rev. 102, 426–436. https://doi.org/10.1016/j.oregeorev.2018.09.022.
Zhong, R., Brugger, J., Tomkins, A.G., Chen, Y., Li, W., 2015. Fate of gold and base metals during metamorphic devolatilization of a pelite. Geochim. Cosmochim. Acta 171, 338–352. https://doi.org/10.1016/j.gca.2015.09.013.
Zuo, Q., Xu, Y., Yu, B., Zhang, C., Zhang, Y., Hou, C., Zhang, L., Sun, M., 2021. NanoSIMS sulfur isotope studies of pyrite from the Early Paleozoic marine shale: Implications for the sedimentary environment. Mar. Pet. Geol. 124, 104802. https://doi.org/10.1016/j.marpetgeo.2020.104802.